9-20-2017

Ambiance-dependent agglomeration and surface-enhanced Raman spectroscopy response of self-assembled silver nanoparticles for plasmonic photovoltaic devices

Jephias Gwamuri
Michigan Technological University

Ragavendran Venkatesan
Madurai Kamaraj University

Mehdi Sadatgol
Michigan Technological University

Jeyanthinath Mayandi
Madurai Kamaraj University

Durdo O. Guney
Michigan Technological University

See next page for additional authors

Journal of Photonics for Energy

PhotonicsforEnergy.SPIEDigitalLibrary.org

Ambiance-dependent agglomeration and surface-enhanced Raman spectroscopy response of self-assembled silver nanoparticles for plasmonic photovoltaic devices

Jephias Gwamuri
Ragavendran Venkatesan
Mehdi Sadatgol
Jeyanthinath Mayandi
Durdu O. Guney
Joshua M. Pearce

SPIE.

Jephias Gwamuri, Ragavendran Venkatesan, Mehdi Sadatgol, Jeyanthinath Mayandi, Durdu O. Guney, Joshua M. Pearce, "Ambiance-dependent agglomeration and surface-enhanced Raman spectroscopy response of self-assembled silver nanoparticles for plasmonic photovoltaic devices," *J. Photon. Energy* **7**(3), 037002 (2017), doi: 10.1117/1.JPE.7.037002.

Ambiance-dependent agglomeration and surface-enhanced Raman spectroscopy response of self-assembled silver nanoparticles for plasmonic photovoltaic devices

Jephias Gwamuri,[a,b,*] Ragavendran Venkatesan,[c] Mehdi Sadatgol,[d] Jeyanthinath Mayandi,[c] Durdu O. Guney,[d] and Joshua M. Pearce[a,d]

[a]Michigan Technological University, Department of Materials Science and Engineering, Houghton, Michigan, United States

[b]National University of Science and Technology, Department of Applied Physics, Bulawayo, Zimbabwe

[c]Madurai Kamaraj University, School of Chemistry, Department of Materials Science, Madurai, India

[d]Michigan Technological University, Department of Electrical and Computer Engineering, Houghton, Michigan, United States

Abstract. The agglomeration/dewetting process of thin silver films provides a scalable method of obtaining self-assembled nanoparticles (SANPs) for plasmonics-based thin-film solar photovoltaic (PV) devices. We show the effect of annealing ambiance on silver SANP average size, particle/cluster finite shape, substrate area coverage/particle distribution, and how these physical parameters influence optical properties and surface-enhanced Raman scattering (SERS) responses of SANPs. Statistical analysis performed indicates that generally Ag SANPs processed in the presence of a gas (argon and nitrogen) ambiance tend to have smaller average size particles compared to those processed under vacuum. Optical properties are observed to be highly dependent on particle size, separation distance, and finite shape. The greatest SERS enhancement was observed for the argon-processed samples. There is a correlation between simulation and experimental data that indicate argon-processed AgNPs have a great potential to enhance light coupling when integrated to thin-film PV. © *2017 Society of Photo-Optical Instrumentation Engineers (SPIE)* [DOI: 10.1117/1.JPE.7.037002]

Keywords: photovoltaics; Raman scattering; plasmonics; agglomeration; self-assembly; thin-film PV; optical properties.

Paper 17048SS received May 29, 2017; accepted for publication Aug. 25, 2017; published online Sep. 20, 2017.

1 Introduction

As-deposited thin metallic films are generally metastable or unstable and readily dewet from a solid substrate when heated even well below their melting temperature.[1,2] The process of agglomeration/dewetting proceeds in two ways: nucleation and growth of holes, and spinodal dewetting.[1,3–5] This process is a relatively economical means of obtaining both simple and complex nanostructures from thin metal films[5–10] compared to traditional methods such as e-beam lithography. While dewetting during film processing has been reported to have undesirable effects on micro- and nanosystems, agglomeration has become the method of choice for catalyzed growth of nanotubes/nanowires and electronic and photonic devices.[3] Dewetting of thin metallic films (both liquid and solid) to obtain mono/multidispersed nanoparticles has been demonstrated with a range of metals including: gold (Au), silver (Ag), nickel (Ni), copper (Cu), and alumina (Al), among others.[1,3–4,10,11] However, Ag film dewetting has been mostly investigated

*Address all correspondence to: Jephias Gwamuri, E-mail: jephias.gwamuri@nust.ac.zw

1947-7988/2017/$25.00 © 2017 SPIE

as a candidate for plasmonic sensing[12–18] and plasmonic-enhanced solar photovoltaic (PV) device[19–31] applications. This is because Ag is generally considered to have the most suitable optical properties for solar cell applications. Silver nanoparticles exhibit highly intense and localized surface plasmon resonances (LSPR) and low absorption in the visible- and near-infrared,[13,32] which is also the spectral region of interest for PV devices. The LSPR of Ag nanoparticles results in electromagnetic field enhancement, which is responsible for the observed surface-enhanced Raman scattering (SERS).[12,13] A detailed discussion on the SERS analysis and the origin of the associated Raman peaks is well-studied and documented in Refs. 33–42. In this work, we focus on further exploiting the agglomeration/dewetting process of thin Ag films on indium tin oxide (ITO) radio frequency (RF) sputtered on glass substrates to obtain self-assembled nanoparticles (SANPs) optimized for plasmonic-based thin film hydrogenated amorphous silicon (a-Si:H) PV devices. This work further investigates the effect of annealing ambiance on; Ag NP average size, circularity, substrate area coverage/particle distribution, optical properties, and SERS responses. In addition, x-ray diffraction (XRD) results are used to discuss the research findings in order to provide guidance for the integration of Ag SANPs with a-Si:H PV devices.

2 Experimental Details

Thin films (average thickness of 18.8 nm) of Ag were deposited using e-beam (KH Frederick EB12) onto ITO/glass substrates previously prepared according to the recipe described in Refs. 43–47. Samples were divided into three batches by annealing temperature: S1 (210°C), S2 (180°C), and S3 (150°C). The samples were further divided based on processing ambiance. The ambiance was varied during annealing of the films to influence both the average nanoparticle size and surface coverage/distribution. The ambiance conditions included argon (Ar), nitrogen (N_2), and vacuum (Vac). The annealing period was kept constant for all samples (1 h) except for those processed under vacuum conditions, which were processed for 2 h (as this time was needed to reach the set temperature of 180°C under vacuum). We focus on results from samples that were processed at 180°C for two reasons. (i) Processing temperature is ideal for AgNPs—PV integration compared to 210°C, which is greater than most p-a-Si:H layer processing temperature. (ii) There are challenges when trying to obtain uniformly distributed AgNPs from thin films processed at lower temperatures (150°C and below).

Surface morphology was characterized with a Hitachi S4700 field-emission scanning electron microscopy and images were processed using ImageJ (imagej.nih.gov) to determine particle size and distribution. Atomic force microscopy (AFM) was performed using a Veeco Dimension 3000 equipment with cantilever tips (Tap300Al-G) on a 1:1 acquisition aspect ratio and roughness analysis was performed on a defect-free region. The absorbance spectra were measured using a Shimadzu UV–vis spectrophotometer (UV2450) and the structural analysis was carried out using a powder PANalytical x-ray diffractometer with CuKa radiation ($k = 1.54$ Å). Raman-scattering SERS measurements were performed in 180-deg backscattering geometry using a LabRamHR800 spectrometer from Horiba Jobin–Yvon equipped with a CCD detector. The samples were excited by 633-nm emission wavelength from a He–Ne laser and the resolution of the spectrometer used was about 0.3 cm^{-1}.

2.1 *Particle Size Analysis*

2.1.1 *Scanning electron microscopy analysis*

SEM analysis was performed to determine ambiance-dependent agglomeration and the results are shown in Figs. 1(a)–1(c). An as-deposited sample in Fig. 1(d) is included for comparison purposes. The dependence of the SANP shape, surface coverage, and size on the processing ambiance is evident from Fig. 1. The SEM analysis further reveals the presence of silver nanoparticles as small finite clusters in all samples; however, there is a vast contrast when it comes to the size and distribution of these clusters. In the case of vacuum-annealed films, the particles are more spherical in shape and uniformly distributed. There are two predominant sizes of particles present—one with small size around 50 nm and larger particles around 140 nm, but the larger

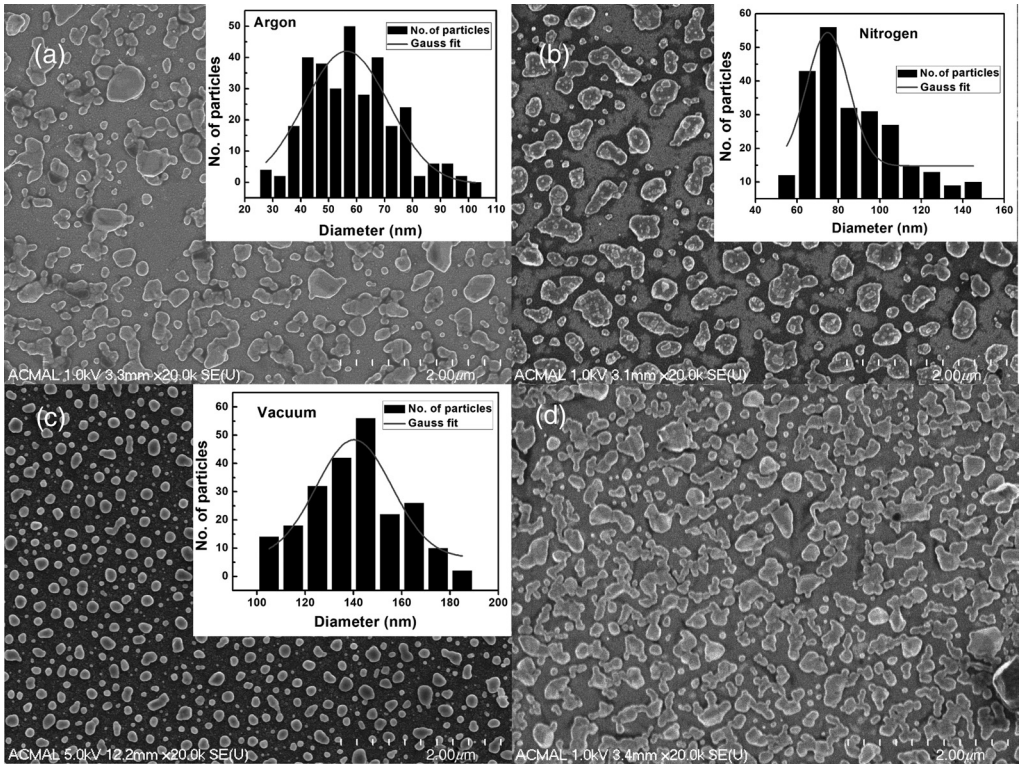

Fig. 1 SEM images showing particle distribution for Ag/ITO/glass samples annealed at 180°C in (a) argon, (b) nitrogen, (c) vacuum, and (d) as-deposited. Insets: histograms showing particle size distribution for varied processing ambiance.

particles are more dominant. For nitrogen-annealed films, the particles are of finite clusters with uniform distribution having irregular shapes and the average calculated particle size is around 77 nm. Argon-annealed samples have a nearly spherical shape with distinguishable particles and some aggregated clusters and the average particle size is around 55 nm.

To facilitate the statistical analysis of the nanostructure size, the Ag nanoparticles were approximated to be a spherical whole. The size histogram of the samples shows that the size variation ranges between 35 and 105 nm for Ar-processed nanostructures, 50 to 150 nm for N_2-processed nanostructures, and 100 to 190 nm for vacuum-processed nanoparticles. Results show that Ag nanostructures processed under Ar ambiance conditions had the largest size variation and hence the most multidispersed nanoparticles. There is less size variance for the NPs processed under N_2 and vacuum ambiance. No evidence of residual nondewetted film was observed from SEM characterization; however, we can only speculate the possibility of some Ag diffusing into the underlying ITO layer during annealing resulting in an optical lossy ITO–Ag alloy layer. The SEM analysis results, together with the XRD, UV–vis average transmittances, and Tauc plot results are summarized in Table 1.

2.1.2 *AFM analysis*

The AFM results were used to complement the SEM analysis and sample results are shown in Fig. 2. Surface roughness analysis showed that the height of the particles varied from 12 to around 130 nm with a root mean roughness of 24 nm. This means the NPs can be approximated to be hemispherical in shape since their diameters range from 60 to 200 nm. The observed particle size/diameter approximates the Gaussian distribution [see Figs. 1(a)–1(c), inset]. For an ideal hemisphere, the diameter/height ratio should be 2 since the diameter is twice the height. In this study, particle height is observed to vary from 12 nm for 60-nm-diameter NPs to 130 nm for 200-nm-diameter particles. However, for the vacuum annealing (150°C), the 140-nm-diameter particles (height = 66 nm) were observed to predominate. The diameter/height ratio

Table 1 Summary of SEM, XRD, UV–vis, and Tauc plot analysis showing average: particle and grain size, transmittance and electronic band gap for samples processed in varied ambience.

	SEM		XRD		UV–vis	
Processing/ambiance	Particle size (nm)	Standard deviation (nm)	2Θ (deg)	Grain size (nm)	Average transmittance (400 to 800 nm) (%)	Band gap (eV)
Argon	56	15	38	20	52	3.70
Nitrogen	75	13	39	20	77	3.86
Vacuum	140	16	38	19	45	3.96
As-deposited	—	—	39	20	66	3.90[a]

[a]The optical bandgap indicated is for the Ag + ITO layer since the Ag film is not continuous.

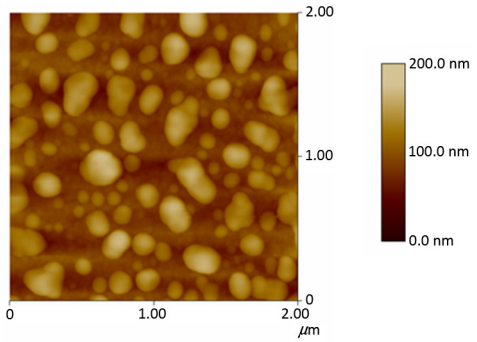

Fig. 2 AFM images showing vacuum-annealed AgNPs on ITO/glass substrate at 150°C. Image scale is 200 nm.

analysis for the three different sizes presents the following values: 5 for small-sized particles (60/12 nm), ~2 for medium-sized particles (140/66 nm), and 1.5 for large-sized particles (200/130 nm), respectively. The trend shows a transition in the evolution of the NP from being thin two-dimensional as-deposited film to quasinanodisc structures (smaller particles) through to hemispherical for medium-sized and most predominant particles with isolated quasispherical particles for large particles. Because of this observation, the hemispherical classification of the particles is statistically valid.

2.2 *Optical Properties*

2.2.1 *UV–vis spectroscopy*

Generally, the N_2-processed NPs exhibit the greatest transmittance while the least transmittance is observed for the vacuum-annealed AgNPs. The low transmittance in the vacuum-processed NPs can be attributed to the presence of defects[3] while these defects are filled by N_2 atoms under the N_2-processed AgNPs, hence the high transmittance is observed for N_2-annealed samples.[1] The presence of large NPs with a high surface coverage for vacuum-processed samples may result in the AgNPs having a shading effect resulting in low-transmittance values. There is a general correlation between the transmittance and reflectance spectra as seen in both Figs. 3(a) and 3(b).

Figure 3(c) shows the UV–vis spectra obtained for the silver deposited on the ITO/glass plates. As-deposited Ag and Ar-annealed Ag samples show only one broad absorption around 400 nm, which corresponds to the typical (LSPR band) LSPR property of Ag nanoparticles, and

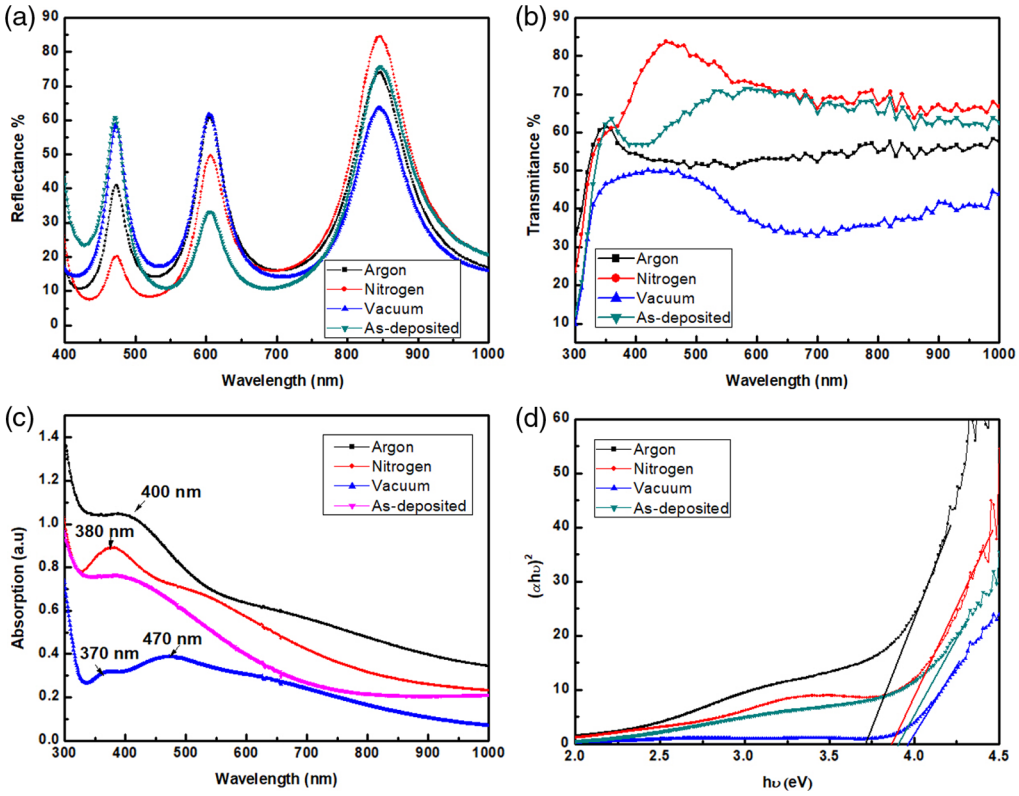

Fig. 3 Ambient dependence of optical and electronic properties for AgNPs: (a) reflectance, (b) transmittance, (c) UV–vis absorption spectra, and (d) Tauc plot for argon, nitrogen, vacuum, and as-deposited samples.

the broad absorption peak implies the broad size distribution of the AgNPs, which is consistent with the SEM characterization. The vacuum-annealed Ag samples show the two LSPR bands located at 370 and 470 nm corresponding to out-of-plane quadrupole resonance and in-plane dipole resonance of the LSPR, respectively,[48] which further confirms the formation of Ag nano-disc-like structures. The same absorption pattern was obtained for the N_2-annealed Ag samples with absorption maxima at 380 and 530 nm, this red shift of the main SPR band of Ag is ascribed to the bigger particle size formed under N_2 annealing condition. Furthermore, the presence of two LSPR peaks at 380 and 530 nm could be resultant from the size distribution of the Ag NPs, since both small and large Ag NPs are in comparable numbers and could give two peaks.

The presence of the broad absorption peak around the 400- to 500-nm region for Ar-processed AgNPs indicates great light harvesting potential in those regions to assist PV response. The band gap is estimated from the absorption spectra using the Tauc plot shown in Fig. 3(d) and the optical band gaps observed for the samples annealed in different ambiances were as follows: Ar, 3.70 eV; N_2, 3.86 eV; vacuum, 3.96 eV; and 3.90 eV for as-deposited Ag + ITO samples. The observed optical band gaps show a strong dependence on the carrier concentration of the film.

2.2.2 *SERS analysis*

Methylene blue (MB) was used as analyte to study the Raman activities of the prepared as-deposited and Ag/ITO annealed under different ambiance conditions (argon, nitrogen, and vacuum) using a 633-nm laser as the excitation signal. Figure 4 shows the SERS spectra response for MB adsorbed on as-deposited Ag/ITO/glass and AgNPs processed at 180°C. The main absorption peaks of the MB solution are located at around 610 and 293 nm (not shown) indicating that all peaks are away from the excitation wavelength, thus the resonant Raman effect is normally expected to be too weak[49] to be observed due to its low concentration, and is buried by the Raman scattering arising from the solvent. The SERS results show the presence of a broad

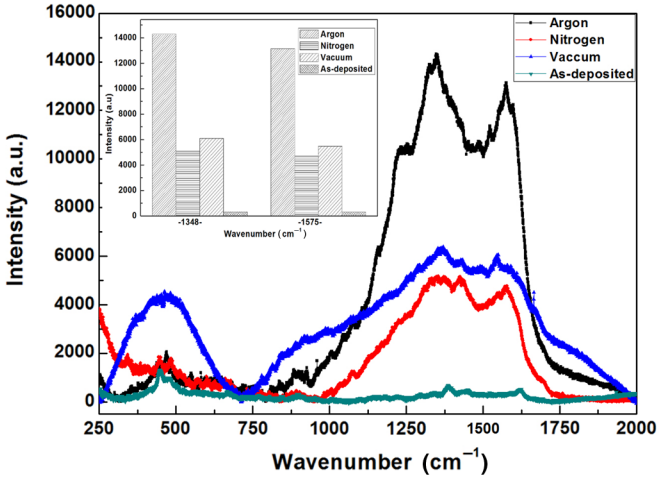

Fig. 4 SERS of Ag/ITO/glass samples (argon, nitrogen, vacuum annealed, and as-deposited) and their intensity variation. Inset: peak intensity variation.

peak at 420 cm^{-1} for only the vacuum-annealed AgNPs sample indicating the predominant presence of large particle size (140 nm on average) in this sample. AgNPs processed under argon ambiance shows the greatest SERS response around 1348 and 1575 cm^{-1}, which is almost twice the response for nitrogen and vacuum-annealed nanoparticles. The presence of the broad UV–vis absorption peak [Fig. 3(c)] observed only for this sample can be attributed to be responsible for the corresponding observed intensity enhancement for Ar-processed AgNPs. The results further show that there is no enhancement for the as-deposited samples. This may be attributed to the absence of finite shape and distance between two nanoparticles/clusters, which is one of the requirements for the SERS enhancement.

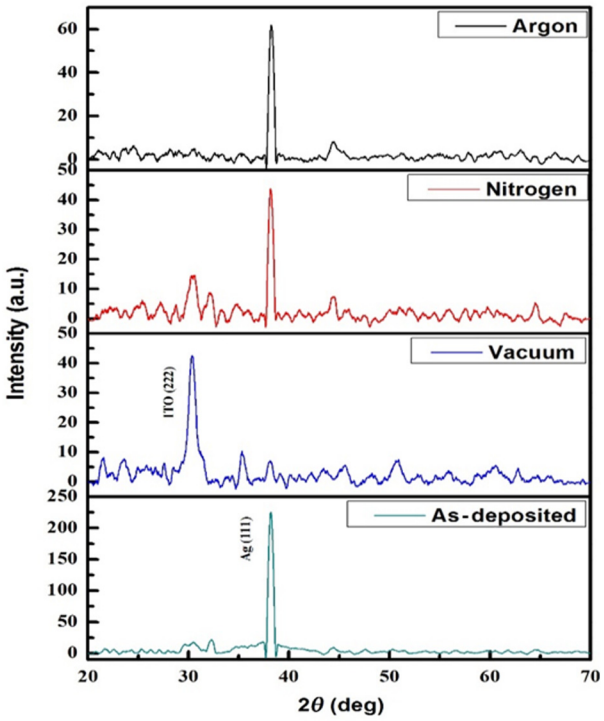

Fig. 5 XRD analysis for argon, nitrogen, and vacuum-annealed (180°C) and as-deposited samples of AgNPs on glass substrate.

2.3 *Structural Analysis*

2.3.1 *XRD analysis*

The crystalline structure was confirmed by the XRD measurements as can be seen in Fig. 5. The XRD analysis results for both as-deposited and processed-AgNPs/ITO/glass show a clear crystalline structure for all samples. Evidently from the XRD results, the dominant peak at 38.2 deg is for Ag (111) (as observed from JCPDS card no: 03-0921) and is present in all study samples. For the case of vacuum-processed NPs, the intensity of the 38.2-deg peak is low and the high intensity peak at 30.3 deg corresponds to ITO (222).[2,49] The same ITO peak can be seen for the nitrogen-processed samples although its intensity is much less compared to the peak intensity observed for the vacuum-annealed samples. This could be attributed to the separation distance between the two nanoparticles/clusters and the finite shape, both of which are absent for the Ar-processed and as-deposited samples. There are also some submissive peaks for Ag visible at 44.4 deg (200) and 64.6 deg (220) in all samples and other submissive peaks at 21.5 deg, 35.4 deg, and 55.8 deg visible in nitrogen- and vacuum-processed samples corresponding to ITO (211), (400), and (611) planes, respectively. The average grain sizes for all samples summarized in Table 1 were determined from the Debye–Scherrer formula for Ag particle to be around 19.7 nm.

3 Modeling and Theoretical Analysis

In order to study the details of optical response of the structure and predict the behavior of the NPs in different situations, a numerical study has been performed. First, absorption spectra for monodispersed nanoparticles with different particle sizes were modeled with a commercial fully vectorial finite-element-based software package COMSOL Multiphysics RF module v5.0 in frequency domain. The geometry consists of a thick glass substrate that has been coated with 70-nm-thick ITO film. The monodispersed nanoparticles were modeled by a periodic array of metallic hemispheres on top the ITO film, see Fig. 6(a). The absorbed power in the metallic hemispheres was found for the case of a normally incident plane wave ranging from 300 to 730 nm.

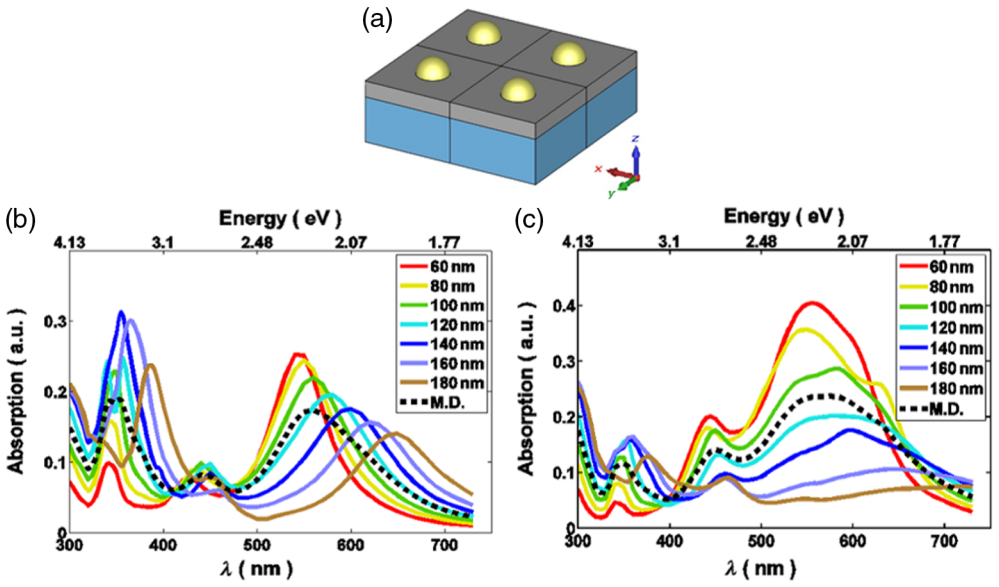

Fig. 6 (a) The geometry used to model the monodisperse AgNPs. Blue shows the glass substrate, ITO is illustrated by the gray layer, and the gold hemispheres represent the NPs. (b) Absorption spectra for monodisperse and multidisperse nanoparticles on glass substrate. Particle size range from 60 to 180 nm. (c) Absorption spectra for monodisperse and multidisperse nanoparticles on a-Si:H substrate. Particle size range from 60 to 180 nm.

The absorption spectrum for multidispersed NPs was calculated by summing over the absorption spectra of the monodispersed AgNPs with different particle sizes, each one weighted with the corresponding relative population in the ensemble. Figures 6(b) and 6(c) show the absorption spectra of mono- and multidisperse AgNPs corresponding to a 18.5-nm-thick Ag film annealed in vacuum. The simulation results [Figs. 6(b) and 6(c)] are in agreement with the UV–vis absorption spectrum experimental data shown in Fig. 3(c).

It is well known that the efficiency of a-Si:H thin film solar cell drops drastically at high wave length (600 nm and greater) because of low absorption of the active intrinsic a-Si:H layer. Several approaches have been proposed to enhance the efficiency of a-Si:H at high wavelengths by incorporating NPs within the cell. Although the improvement in overall device performance is due to contributions from different phenomena such as diffraction, electromagnetic field enhancement, and light trapping mechanisms, for effective absorption in the higher wavelength region, the NPs must resonate at one or more frequencies within this region. It is, therefore, crucial that the multidispersed nanoparticles prepared by the method described in this paper exhibit resonances within the region of interest when incorporated in a-Si:H thin film solar cell.

To investigate the effect of the substrate on the NP resonances, the model file was updated to a-Si:H as the substrate and the same procedure described earlier was repeated to obtain the absorption spectra of multidispersed different sized AgNPs on a-Si:H substrate. Figure 6(c) shows the absorption spectra of mono- and multidispersed NPs on a-Si:H substrate with 70-nm ITO spacer layer. Red-shift of NP resonance frequency in response to increase in refractive index of the substrate has been studied extensively.[50–57] In the case of multidispersed NPs, as shown by the simulation results [Fig. 6(c)], the resonance frequency of AgNPs shifts from 350 to around 600 nm and at the same time the resonance became broader, which is very appealing for plasmonic solar cell application.[19–23,58]

4 Conclusion

In this study, AgNPs of different sizes and surface coverage were synthesized using ambiance-dependent agglomeration of e-beam evaporated silver thin films (18.5 to 25 nm). The influence of different processing ambiance conditions was observed on both NPs morphology and optical properties. Results here show that the conditions to obtain the greatest SERS intensity enhancement of up to 14 times is possible for 18.5-nm Ag film samples processed in argon ambiance relative to vacuum-processed films. Further results from simulations on NP optical response consolidate the observed experimental data. A strong correlation is observed between processing conditions, particle sizes, shapes, and their optical response (both UV–vis absorption and SERS). From the results we infer that for the enhancement of SERS, the particles need not to be of spherical but should have finite shape and the separation distance between them is more crucial for the enhancement to be observed. The high plasmonic enhancement in SERS occurs when the separation distance between the two particles is minimum (less than 20 nm).

There is a clear observed relationship between particle size and resonance frequency indicated by the red-shifting of the resonances with the increasing particle size. XRD analysis reveals both the presence of polycrystalline bcc ITO and fcc Ag. No Ag–Sn phases are observed in the results showing that there was no alloying between the Ag and Sn (from ITO) during the annealing process. The ability to mass-fabricate NPs economically and the ability to deliberately tailor their optical response through the use of different ambiance conditions present the greater opportunities for targeted application areas such as thin film PV devices, plasmonic photothermal therapy, and plasmonic sensing.

Disclosures

The authors declare no competing financial interests.

Acknowledgments

This work was supported by the National Science Foundation under Grant Award No. CBET-1235750 and the Fulbright S&T Award. J. Mayandi thanks the DST for the financial support

Reference No. DSTSERB/F/1829/2012-2013. The authors thank UGC-UPE Programme of Madurai Kamaraj University, India, for providing micro-Raman facility.

References

1. J. Bischof et al., "Dewetting modes of thin metallic films: nucleation of holes and spinodal dewetting," *Phys. Rev. Lett.* **77**(8), 1536–1539 (1996).
2. D. J. Srolovitz and M. G. Goldiner, "The thermodynamics and kinetics of film agglomeration," *JOM* **47**, 31–36 (1995).
3. C. V. Thompson, "Solid-state dewetting of thin films," *Annu. Rev. Mater. Res.* **42**, 399–434 (2012).
4. H. Krishna et al., "Thickness-dependent spontaneous dewetting morphology of ultrathin Ag films," *Nanotechnology* **21**(15) 155601 (2010).
5. S. Herminghaus et al., "Spinodal dewetting in liquid crystal and liquid metal films," *Science* **282**(5390), 916–919 (1998).
6. A. Atena and K. Mikhail, "Thermocapillary effects in driven dewetting and self-assembly of pulsed-laser-irradiated metallic films," *Phys. Rev. B* **80**(7), 075402 (2009).
7. C. Favazza et al., "Robust nanopatterning by laser-induced dewetting of metal nanofilms," *Nanotechnology* **17**(16), 4229–4234 (2006).
8. J. Trice et al., "Novel self-organization mechanism in ultrathin liquid films: theory and experiment," *Phys. Rev. Lett.* **101**(1), 017802 (2008).
9. Y. F. Guan et al., "Pulsed laser dewetting of nickel catalyst for carbon nanofiber growth," *Nanotechnology* **19**(23), 235604 (2008).
10. J. Boneberg et al., "Jumping nanodroplets: a new route towards metallic nano-particles," *Appl. Phys. A* **93**(3), 415–419 (2008).
11. R. Liu et al., "Lithography-free fabrication of silicon nanowire and nanohole arrays by metal-assisted chemical etching," *Nanoscale Res. Lett.* **7**(1), 1–8 (2013).
12. M. Quinten et al., "Electromagnetic energy transport via linear chains of silver nanoparticles," *Opt. Lett.* **23**(17), 1331–1333 (1998).
13. K. A. Willets and R. P. Van Duyne, "Localized surface plasmon resonance spectroscopy and sensing," *Annu. Rev. Phys. Chem.* **58**, 267–297 (2007).
14. D. L. Jeanmaire and R. P. Van Duyne, "Surface Raman spectro-electrochemistry: part I. Heterocyclic, aromatic, and aliphatic amines adsorbed on the anodized silver electrode," *J. Electroanal. Chem. Interfacial Electrochem.* **84**(1), 1–20 (1977).
15. C. L. Haynes et al., "Surface-enhanced Raman sensors: early history and the development of sensors for quantitative biowarfare agent and glucose detection," *J. Raman Spectrosc.* **36**(6–7), 471–484 (2005).
16. G. C. Schatz et al., "Electromagnetic mechanism of SERS," in *Surface-enhanced Raman Scattering*, pp. 19–45, Springer, Berlin, Heidelberg (2006).
17. C. R. Yonzon et al., "A glucose biosensor based on surface-enhanced Raman scattering: improved partition layer, temporal stability, reversibility, and resistance to serum protein interference," *Anal. Chem.* **76**(1), 78–85 (2004).
18. E. J. Zeman and G. C. Schatz, "An accurate electromagnetic theory study of surface enhancement factors for silver, gold, copper, lithium, sodium, aluminum, gallium, indium, zinc, and cadmium," *J. Phys. Chem.* **91**(3), 634–643 (1987).
19. H. A. Atwater and A. Polman, "Plasmonics for improved photovoltaic devices," *Nat. Mater.* **9**(3), 205–213 (2010).
20. S. Pillai et al., "Surface plasmon enhanced silicon solar cells," *J. Appl. Phys.* **101**(9), 093105 (2007).
21. K. R. Catchpole and A. Polman, "Design principles for particle plasmon enhanced solar cells," *Appl. Phys. Lett.* **93**(19), 191113 (2008).
22. F. J. Beck et al., "Tunable light trapping for solar cells using localized surface plasmons," *J. Appl. Phys.* **105**(11), 114310 (2009).
23. J. Gwamuri, D. Ö. Güney, and J. M. Pearce, "Advances in plasmonic light trapping in thin-film solar photovoltaic devices," in *Solar Cell Nanotechnology*, pp. 241–269, John Wiley & Sons, Inc., Hoboken, New Jersey (2013).

24. A. Vora et al., "Exchanging ohmic losses in metamaterial absorbers with useful optical absorption for photovoltaics," *Sci. Rep.* **4**, 4901 (2014).
25. A. Vora et al., "Multi-resonant silver nano-disk patterned thin film hydrogenated amorphous silicon solar cells for Staebler–Wronski effect compensation," *J. Appl. Phys.* **116**(9), 093103 (2014).
26. F. J. Tsai et al., "Absorption enhancement of an amorphous Si solar cell through surface plasmon-induced scattering with metal nanoparticles," *Opt. Express* **18**(102), A207–A220 (2010).
27. R. Santbergen et al., "Application of plasmonic silver island films in thin-film silicon solar cells," *J. Opt.* **14**(3), 024010 (2012).
28. R. Santbergen et al., "A-Si: H solar cells with embedded silver nanoparticles," in *35th IEEE Photovoltaic Specialists Conf. (PVSC)*, pp. 000748–000753 (2010).
29. A. Lin et al., "An optimized surface plasmon photovoltaic structure using energy transfer between discrete nano-particles," *Opt. Express* **21**(101), A131–A145 (2013).
30. F. J. Beck et al., "Asymmetry in photocurrent enhancement by plasmonic nanoparticle arrays located on the front or on the rear of solar cells," *Appl. Phys. Lett.* **96**(3), 033113 (2010).
31. X. Chen et al., "Broadband enhancement in thin-film amorphous silicon solar cells enabled by nucleated silver nanoparticles," *Nano Lett.* **12**(5), 2187–2192 (2012).
32. C. Langhammer et al., "Absorption and scattering of light by Pt, Pd, Ag, and Au nanodisks: absolute cross sections and branching ratios," *J. Chem. Phys.* **126**(19), 194702 (2007).
33. A. Matikainen et al., "Atmospheric oxidation and carbon contamination of silver and its effect on surface-enhanced Raman spectroscopy (SERS)," *Sci. Rep.* **6**, 37192 (2016).
34. N. Colthup, *Introduction to Infrared and Raman Spectroscopy*, Elsevier, Burlingtons, New Jersey (2012).
35. E. V. Efremov, F. Ariese, and C. Gooijer, "Achievements in resonance Raman spectroscopy: review of a technique with a distinct analytical chemistry potential," *Anal. Chim. Acta* **606**, 119–134 (2008).
36. C. L. Evans and X. S. Xie, "Coherent anti-Stokes Raman scattering microscopy: chemical imaging for biology and medicine," *Annu. Rev. Anal. Chem.* **1**, 883–909 (2008).
37. E. Le Ru and P. Etchegoin, *Principles of Surface-enhanced Raman Spectroscopy: and Related Plasmonic Effects*, Elsevier, San Diego, California (2008).
38. A. Campion et al., "On the mechanism of chemical enhancement in surface-enhanced Raman scattering," *J. Am. Chem. Soc.* **117**, 11807–11808 (1995).
39. N. Valley et al., "A look at the origin and magnitude of the chemical contribution to the enhancement mechanism of surface-enhanced Raman spectroscopy (SERS): theory and experiment," *J. Phys. Chem. Lett.* **4**, 2599–2604 (2013).
40. K. Kneipp, M. Moskovits, and H. Kneipp, *Surface-Enhanced Raman Scattering: Physics and Applications*, Springer Science and Business Media, Berlin, Heidelberg (2006).
41. S. S. Masango et al., "High-resolution distance dependence study of surface-enhanced Raman scattering enabled by atomic layer deposition," *Nano Lett.* **16**, 4251–4259 (2016).
42. S. Lindroos and M. Leskelä, *Solution Processing of Inorganic Materials*, in D. Mitzi, Ed., pp. 239–270, John Wiley & Sons, Hoboken, New Jersey (2009).
43. S. A. Knickerbocker, "Estimation and verification of electrical and optical properties of indium-tin-oxide based on energy band diagrams," PhD Thesis, Michigan Technological University, Houghton, Michigan (1995).
44. T. S. Lim, MS Thesis, Michigan Technological University, Houghton, Michigan (1997).
45. J. Gwamuri et al., "Limitations of ultra-thin transparent conducting oxides for integration into plasmonic-enhanced thin-film solar photovoltaic devices," *Mater. Renewable Sustainable Energy* **4**(3), 12 (2015).
46. J. Gwamuri et al., "Influence of oxygen concentration on the performance of ultra-thin RF magnetron sputter deposited indium tin oxide films as a top electrode for photovoltaic devices," *Materials* **9**(1), 63 (2016).
47. J. Gwamuri et al., "A new method of preparing highly conductive ultra-thin indium tin oxide for plasmonic-enhanced thin film solar photovoltaic devices," *Sol. Energy Mater. Sol. Cells* **149**, 250–257 (2016).

48. T. Tan et al., "LSPR-dependent SERS performance of silver nanoplates with highly stable and broad tunable LSPRs prepared through an improved seed-mediated strategy," *Phys. Chem. Chem. Phys.* **15**(48), 21034–21042 (2013).
49. I. Hotovy et al., "Structural characterization of sputtered indium oxide films deposited at room temperature," *Thin Solid Films* **518**(16), 4508–4511 (2010).
50. M. Marikkannan et al., "Effect of ambient combinations of argon, oxygen, and hydrogen on the properties of DC magnetron sputtered indium tin oxide films," *AIP Adv.* **5**(1), 017128 (2015).
51. J. Yun et al., "Preparation of flexible organic solar cells with highly conductive and transparent metal-oxide multilayer electrodes based on silver oxide," *ACS Appl. Mater. Interfaces* **5**(20), 9933–9941 (2013).
52. G. N. Xiao and S. Q. Man, "Surface-enhanced Raman scattering of methylene blue adsorbed on cap-shaped silver nanoparticles," *Chem. Phys. Lett.* **447**(4), 305–309 (2007).
53. J. Z. Zhang, "Optical properties of metal nanomaterial," in *Optical Properties and Spectroscopy of Nanomaterials*, J. Z. Zhang, Ed., pp. 205–235, World Scientific Publishing Company, Inc., Hackensack, New Jersey (2009).
54. L. J. Sherry et al., "Localized surface plasmon resonance spectroscopy of single silver nanocubes," *Nano Lett.* **5**(10), 2034–2038 (2005).
55. L. J. Sherry et al., "Localized surface plasmon resonance spectroscopy of single silver triangular nanoprisms," *Nano Lett.* **6**(9), 2060–2065 (2006).
56. K. L. Kelly et al., "The optical properties of metal nanoparticles: the influence of size, shape, and dielectric environment," *J. Phys. Chem. B* **107**(3), 668–677, (2003).
57. O. Kvítek et al., "Noble metal nanostructures influence of structure and environment on their optical properties," *J. Nanomater.* **2013**(2013), 743684 (2013).
58. P. Spinelli et al., "Plasmonic light trapping in thin-film Si solar cells," *J. Opt.* **14**(3), 024002 (2012).

Jephias Gwamuri received his PhD in materials science and engineering from Michigan Technological University. He is a lecturer in the Applied Physics Department, National University of Science and Technology (NUST), Bulawayo, Zimbabwe. His current research activities include low-cost open-source three-dimensional printing and solar PV devices fabrication and characterization, innovative transparent conducting oxides/electrodes, and energy storage materials. He is a current member of OSA, SPIE, and TMS among other professional societies. He is also affiliated with the Open Sustainability Technology Research Group (MOST) at Michigan Technological University and the lead investigator on the Solar Cell Research Group at NUST.

Ragavendran Venkatesan received his BSc degree from Periyar University, Salem, India, in 2009, his MSc degree from Bharathidasan University, Tiruchirappali, India, in 2011, both in physics, and his MPhil degree in materials science from Madurai Kamarj University, Madurai, India, in 2012. He is currently working toward his PhD in physics in the Department of Materials Science, School of Chemistry, Madurai Kamaraj University. His current research includes porous silicon for photovoltaic application and plasmonics.

Mehdi Sadatgol received his PhD in electrical engineering and his MS degree in applied physics from Michigan Technological University in 2016. He is currently in the Department of Electrical Engineering at Michigan Technological University and is affiliated with the vehicle R&D Group at Harada Industry of America. His research interests include electromagnetic theory, metamaterials, solar photovoltaic, quantum optics, and vehicular communication.

Jeyanthinath Mayandi is working as an assistant professor in the Department of Materials Science, School of Chemistry, Madurai Kamaraj University, Madurai, India, from 2010. His main areas of research interest are renewable energy materials and devices, plasmonics, and metal oxides and semiconductors for biomedical applications.

Durdu O. Guney is an associate professor in the Department of Electrical and Computer Engineering at Michigan Technological University. His research interests are metamaterials,

plasmonics, solar cells, quantum computing, communications and cryptography, photonic crystals and fibers, acoustic bandgap materials, and microoptoelectromechanical systems. His current research activities include subdiffraction limited imaging, plasmonic solar photovoltaic cells, and quantum manipulation of light with metamaterials.

Joshua M. Pearce is a professor cross-appointed in the Department of Materials Science and Engineering and in the Department of Electrical and Computer Engineering at Michigan Technological University, where he runs the Open Sustainability Technology Research Group. His research concentrates on the use of open source appropriate technology to find collaborative solutions to problems in sustainability and poverty reduction. His research spans the areas of electronic device physics and materials engineering of solar photovoltaic cells and RepRap three-dimensional printing, but also includes applied sustainability and energy policy.